Simulations of current transport phenomena in ferroelectric tunnel junctions

IVAN LUBAR
MASTER´S THESIS
DEPARTMENT OF ELECTRICAL AND INFORMATION TECHNOLOGY
FACULTY OF ENGINEERING | LTH | LUND UNIVERSITY

Simulations of current transport phenomena in ferroelectric tunnel junctions

Ivan Lubar

Supervisor: Mattias Borg

Examiner: Erik Lind

Department of Electrical and Information Technology
Lund University
June 17, 2022

Abstract

Ferroelectric memories pose as a potential candidate as resistive memory devices that could be used for in-memory computing and artificial synapses. One promising type of ferroelectric memory device is the ferroelectric tunnel junction (FTJ). The basic functionality of a FTJ device is based upon the fact that ferroelectric materials display two distinct polarization states which could be switched in order to achieve two resistance states in the device.

There are several current pathways contributing to the current in a FTJ and the exact mechanisms are not entirely understood. There is a need for a numerical model, where electronic band structure and defect current pathways are considered, that includes physically well grounded fitting parameters. In this thesis two such models for the trap-assisted tunneling (TAT) current are investigated and fitted to experimental data. The first model is based upon occupational probability in the metal electrodes and transmission probabilities given by the WKB approximation. The second model utilizes Fermi's golden rule in order to estimate transition rate.

Both models in general display unsatisfactory results in terms of reproducing and fitting to experimental data. The second model displays some promising results once empirical constants are introduced which indicate towards a certain accuracy in the parameters and models used. The main deviations are believed to stem from an overly simplified bandstructure model and normalization problems.

Popular Science Summary

In modern day technologies the demand for high performance memory solutions increases rapidly as modern technologies and applications are data driven. The ever increasing need for larger amounts of data and processing speeds has led to technological bottlenecks. The computational speed today is limited by the speed at which data could be fetched from memory. The solution? Perform computations in the memory directly and, thus reduce the time needed to transfer the memory to the processors. This is known as in-memory computation, and it probably partly will serve as the solution for the worlds data processing problems. The performance of modern day memory devices is lacking for them to be utilized for in-memory computation. This opens up a whole new field in search of better, faster and more advanced memory devices.

One promising type of future memory device is the ferroelectric tunnel junction (FTJ). The FTJ consists of two metal electrodes with a ferroelectric material sandwiched in between them. The basic functionality of an FTJ device is based upon the fact that ferroelectric materials display two distinct polarization states, that could be switched in order to achieve two different resistance states in the device which are needed in memory applications. The two resistance states are the binary, 1 and 0, used in computers. Polarization could in simple terms be explained as the separation of charge carriers in a certain direction. The phenomena behind the current transport in an FTJ is quantum mechanical tunneling. Quantum mechanical tunneling is a phenomenon where a particle can travel through a energy barrier even though it does not posses the sufficient energy to do so, an impossibility in classical physics! It might sound like the mechanics behind the current in FTJs are entirely understood, but this is not the case. There is in fact a need for good models describing the physics in an FTJ in order to aid our understanding of the device and how to optimize it for suitable applications. The idea of finding good model was the purpose of this project. The focus was has been on trying to implement such a model for specific the dominating current mechanism in the FTJ and get it to match data from real devices. However the task proved difficult and the model that was used was too simple in order to give represent the physics of the device accurately.

Acknowledgements

I would first of all like to express my gratitude towards my supervisor Mattias Borg, for supporting me throughout the course of the project and always being easily available for questions and guidance. He has shown me great patience despite practical difficulties in arranging meetings on my part. I also want to thank my examiner, Erik Lind, for the valuable remarks for the final version of the thesis which provided me with valuable insights to the subject.

I want to like to thank all those dear to me, my parents, my sister, friends and my girlfriend for all the support, especially in the most stressful times during this project. Your support has been invaluable to me.

Most of all I want to express my most sincere gratitude towards my dear friend Joseph, who has helped me tremendously in my studies, but even more so in life in general. Thank you.

Contents

Chapter 1

Introduction

1.1 Background

In modern day technologies the demand for high performance memory solutions increases rapidly as modern workloads are data driven. The ever increasing need for larger amounts of data and processing speeds has led to technological and computational bottlenecks. The computational speed today is limited by the speed at which data could be fetched from memory. This is is known as the von-Neumann bottleneck and for every year the performance gap between the processors and memory devices increases [1]. A solution to the performance gap could be in-memory computing. In-memory computing entails moving the computation into the memory itself. This solution requires resistive memory technologies in order to perform the In-memory computations [2].

1.2 Ferroelectric tunnel junction

Ferroelectric memories are potential candidates as resistive memory devices that could be used for in-memory computing and artificial synapses [4]. One promising type of ferroelectric memory device is the ferroelectric tunnel junction (FTJ). FTJs display promising qualities for non-volatile resistive memories, meaning memory can be retained without power supply [3]. They also exhibit fast switching, low power consumption and great on/off ratio all which are desirable for high performing memory devices. The basics behind the FTJ was already discovered as early as 1971[5]. What limited the endeavour of creating FTJs back then was the inability to manufacture thin high-quality ferroelectrics which could be integrated into CMOS technology. With time the technological and scientific advances made it possible to fabricate thin films of ferroelectric

material and integrate it into chips [4]. However, the big breakthrough came with the discovery of ferroelectricity in hafnium oxide in 2011 which opened up a lot of possibilities for ferroelectric memories, as hafnium oxide already was a well established material used in CMOS processes [4].

The operation of FTJs is, as the name suggests, based upon the physical phenomenon of ferroelectricity. Ferroelectric materials usually display two distinct polarization states which are sustained by the material without an external electric field [4]. In an FTJ these polarization states are utilized by sandwiching a thin film of ferroelectric insulator between two metal electrodes which makes the ferroelectric material act as a tunneling barrier. By changing the polarization, the barrier height is modified, which in turn changes the current flowing through the FTJ. Because of the asymmetry of a physical property in the metal electrodes termed the screening length, different barrier heights are achieved depending on the direction of the polarization which gives rise to two separate resistance states [4]. High separation contrast between the resistance states is desirable for memory applications [3].

From the name it could be assumed that the main current transport mechanism in FTJs is tunneling, but there are several current pathways contributing to the current in an FTJ, and the exact mechanisms are not entirely understood. There exists phenomenological models to model and fit the current to experimental data but non-physical fitting parameters are required for this. Thus, there is a need for a numerical model where electronic band structure and defect current pathways are considered that includes physically well grounded fitting parameters.

1.3 Aim of the thesis

The aim of this Master's thesis work is to examine a numerical model mentioned in the previous section. Tunneling and thermal emission is modelled based on the Tsu-Esaki model via a transmission coefficient obtained through the WKB approximation. An initial simulation tool was implemented by the supervisor in MATLAB, which was cleaned up and improved to also include trap-assisted tunnelling. Evaluation of the models will be based on fitting to experimental data from already fabricated FTJ devices.

Chapter 2

Theory and model

This section aims to present the theory behind the models that were implemented to be able to simulate the current of the FTJ. Since the theoretical background basically is, or is closely related to the model in terms of constants and equations governing the behaviour of the materials, this section treats them as one.

2.1 Physical structure of the FTJ device

The FTJ that was modeled is a metal-ferroelectric-metal (MFM) structure where the ferroelectric (FE) insulator, in our case the $Hf_{0.5}Zr_{0.5}O_2$ (HZO), is sandwiched between two metal electrodes. One top electrode (TE) and bottom electrode (BE) as shown in figure 2.1. The metal electrodes which were modeled are tungsten (W) and titanium nitride (TiN). A voltage was applied to the top electrode which altered the current passing through the device by changing the bandstructure of the device. The exact and relevant dimension and specifics of the materials used and modeled will be presented in later sections.

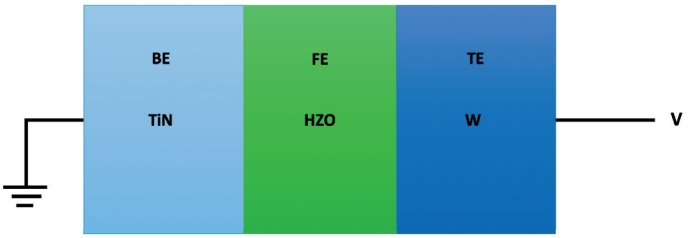

Figure 2.1: Schematic diagram of the FTJ that was modelled, displaying the electrodes and ferroelectric used.

2.2 Model of the metal contacts

In order to model the current transport and calculate the bandstructure of the FTJ correctly, the physical properties need to be well defined. The relevant physical properties are then used as parameters in the model of the metal contacts used in the simulations. The electron model which is used to estimate some of the physical parameters of the metal is the nearly free electron (NFE) model.

The nearly free electron model is a mathematical model which describes the motion of electrons within a periodic potential such as a crystal lattice. This mathematical model allows for the calculation of the bandstructure in certain materials and the way they are distributed as a function of the wavevector [6]. The way that the NFE model is implemented in the model of the metal contacts (and the HZO) is by using an effective mass in the equations governing the distribution and velocities of the electrons in the metal. This is an approximation, where the energy of the electrons in the NFE model could be described using the free electron energy dispersion relation, corrected for with an effective mass [6]. The energy as a function of the wave vector for the NFE model is given by

$$E(k) = \frac{\hbar^2 k^2}{2m^*} \tag{2.1}$$

where m^* is the effective mass, $\hbar$ the reduced Planck's constant and k the wave vector. However, this approximation is only valid close to the conduction band bottom or valence band top [6]. However, in a metal the Fermi energy will relatively high compared to the conduction band. This

might source of inaccuracy in the model as this approximation would be precise for a slightly filled band in the metal [7]. In order to obtain an accurate calculation of the band structure in metals a more thorough and rigorous description of the NFE model is needed [7]. The energy-wave vector dependence can be visualized in figure 2.2.

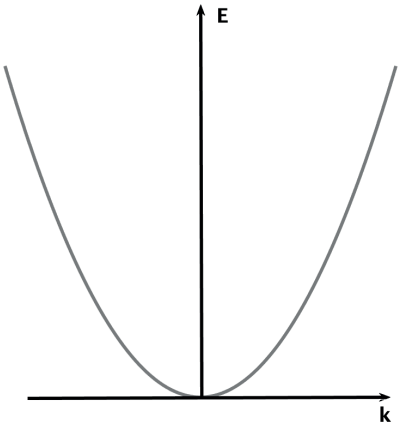

Figure 2.2: Energy as a function of the wave vector for the NFE model.

From equation 2.1 the expression for the velocity can be found which will be shown in later sections. The effective mass is also needed to calculate the density of states (DOS).

2.2.1 Effective masses and the electron densities of the metals

The value of the effective mass for the different metals is extracted from the specific heat at low temperatures, this because at low temperatures the excitement of electrons is the main contributor to the specific heat of a material [6]. The equations used for the extraction of the effective mass are the following [8],

$$c_v = \gamma + AT^2 \tag{2.2}$$

where c_v is the specific heat at constant volume, T is the temperature, A a constant and γ is the electron specific heat coefficient and is given by

$$\gamma = \frac{\pi^2 k_B^2 n}{2E_F} \tag{2.3}$$

which could be rewritten as

$$E_F = \frac{\pi^2 k_B^2 n}{2\gamma} \tag{2.4}$$

where E_F is the Fermi energy of the metal and n is the conduction band free electron density of the metal and k_B is the Boltzmann constant. The Fermi energy relative to the band bottom in the metals is given by [6]

$$E_F = \frac{\hbar^2}{2m^*}(3\pi n)^{2/3} \tag{2.5}$$

where m^* is the effective mass of the electrons in the metal. Now using equations 2.5 and 2.4 one could obtain the following expression for the estimation of the effective electron mass

$$m^* = \frac{\hbar^2 \gamma}{k_B^2}\left(\frac{3}{\pi}\right)^{2/3} n^{-1/3} \tag{2.6}$$

Hence an accurate estimation of the electron density is needed in order to obtain a proper value. The free electron density could be calculated from the following equation [10].

$$n = \frac{N_A \rho}{M} k \tag{2.7}$$

where N_A is Avogadro's constant, ρ is the density of the metal, M the molar mass and k the number of delocalized electrons per atom that add to the free electron density. Tungsten's electron configuration is [Xe]6s^{2}4f^{14}5d^4 in atomic form. However in crystal form the electron configuration of tungsten is [Xe]6s^{1}4f^{14}5d^5 which gives k = 1 since only the s-orbital electrons become delocalized and conduct current [11]. With the density being 19.35 g/cm^3 and the molar mass 183.8 u the electron density for tungsten was calculated to be $6.3 \cdot 10^{28}$ m^{-3} [12][13].

The electron specific heat coefficient in tungsten is according to the work of Loucks 67.8 $Jkg^{-1}K^{-1}$ [9]. Using the estimated electron density value for tungsten and the electron specific heat coefficient one could using equation 2.6 estimate the effective electron mass to be 1.06.

Since TiN is a compound it is hard to estimate the effective mass and electron density using the same approach as for tungsten. An estimate for the effective mass and electron density for TiN was taken from the work of Walker et al. and are estimated to be m^* = 2.7 and n_{TiN} = $5.3 \cdot 10^{28}$ m^{-3} [14].

2.2.2 Dielectric constant and screening length

In order to be able to calculate a precise and accurate band structure of the FTJ, which is crucial in order to model the current properly, the dielectric constant and the Thomas-Fermi screening lengths need to be estimated. As it happens these physical parameters are closely related. In order to be able to calculate the dielectric constant of the metals the Thomas-Fermi dielectric function needs to be found [15]. The dielectric function describes how a material is affected by an electromagnetic field. The Thomas-Fermi dielectric function is derived by considering the screening of a positive charge by an electron gas [8]. By assuming that the chemical potential (Fermi level) is constant and that the potential varies slowly, meaning that that electrons respond as if the potential was electrostatic, one could derive the Thomas-Fermi dielectric function to be [15]

$$\varepsilon(\omega = 0, \mathbf{k}) = 1 + \frac{k_s^2}{k^2} \tag{2.8}$$

where k is the wavevector and k_s is given by[15]

$$k_s^2 = \frac{4}{a_0}\left(\frac{3n}{\pi}\right)^{1/3} \tag{2.9}$$

where a_0 is the Bohr radius which is written as

$$a_0 = \frac{4\pi\varepsilon_0\hbar}{m_e q^2} \tag{2.10}$$

where ε_0 is the vacuum permittivity and q the electron unit charge. In our model we use the modified Bohr radius a_0' = a_0/m_{eff}. The dielectric constant for the metals is calculated by setting k in equation 2.8 to the Fermi wavevector

$$k_f = \frac{\sqrt{2m^* E_F}}{\hbar} \tag{2.11}$$

The Thomas-Fermi screening length of the metal is given by $l = 1/k_s$ [15]. What the Thomas-Fermi screening implies physically is how well the electrons in a material screen a positive charge. In our model this happens when e.g positive charge accumulates on the side of the ferroelectric which attracts negative charges (electrons) in the metal as in figure 2.3. The negative charges that accumulate on the metal-HZO interface will then screen the positive potential, hence causing less electrons to be attracted to the interface. The accumulation of electrons causes a bending of the

conduction band in the metal which then affects the bandstructure of the device. The amount of electrons accumulated on the interface decreases with a gradient but this is approximated with a certain length being the screening length parameter denoted by l in figure 2.3 [16].

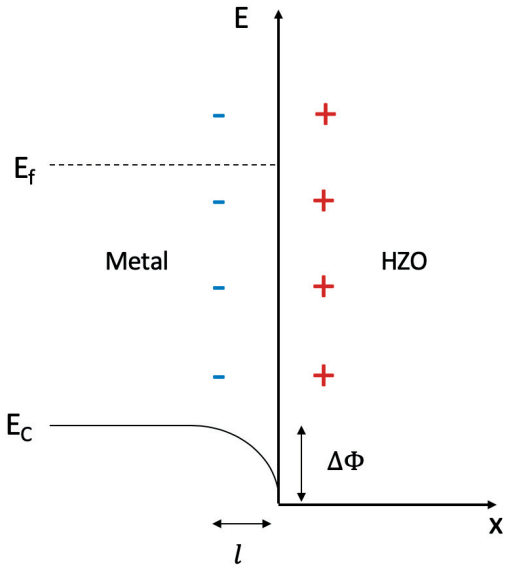

Figure 2.3: Schematic of the effect of accumulation of charges at Metal-HZO interface.

Both the screening length and dielectric constant affect bandstructure of the device, which is induced by the polarization of the HZO [16], which then impacts the current through the device. The way they impact the bandstructure will be presented in later sections.

2.2.3 Remaining physical parameters and summary of constants

The most fundamental physical parameter in order to calculate the band structure is the workfunction for the metal. The difference between the workfunction and the electron affinity of the ferroelectric gives the height of the barrier [17]. The work function of a metal is defined as the minimum energy needed to remove an electron from the metal [18]. For tungsten the value is found in literature to be 4.55 eV [19]. For TiN the workfunction was set in order to match typical barrier height found in literature, which is around 1.8 eV in one of the polarization directions [20]. From this workfunction of TiN was estimated to be approximately 4.37 eV. However, since TiN is a compound it is difficult to know whether the composition used in the modelled devices match those found in literature so the value might vary significantly as much as 4.25 - 4.55 eV [24] [25]. In a

study by Athle et al. similar values were used in order to model the current transport in the devices studied [10]. The workfunction of TiN will be used as a fitting parameter in the simulations.

Below a summary of the physical parameters in the metal are presented in table 2.1.

Table 2.1: Summary of the physical constants in the metal electrodes

Metal	Workfunction (eV)	Effective mass	Free electron density (m^{-3})
W (TE)	4.55	1.06	$6.3 \cdot 10^{28}$
TiN (BE)	4.37	2.7	$5.3 \cdot 10^{28}$

2.3 Model of the HZO

As in the case of the metal models, the physical properties of the HZO are needed in order to calculate a proper bandstructure which will enable a good model of the current through the device. At the basis of an FTJs functionality lies the ferroelectric properties of the ferroelectric insulator sandwiched between the metals.

2.3.1 Ferroelectricity and polarization

Polarization is a measure of the dipole moment per unit volume in a material. When an electric field is applied to a dielectric, the field will induce a dipole moment in the polar molecules of the material which causes the dipoles to align themselves to the electric field [23]. This response creates surface charges in the material, since the positive and negative charges of the molecules even out elsewhere in the material due to the alignment of the dipoles. The dielectric is said to be polarized when the surface charges are generated. Between the surface charges an electric field will emerge which is opposite to the polarization of the material.

A ferroelectric material can be defined as a material or crystal which displays a constant spontaneous polarization without any presence of an electric field [21]. The polarization of the ferroelectric can be reversed by applying an electric field to it. In order for materials to be ferroelectric they must exhibit a non-centrosymmetric crystal structure. The non-centrosymmetric crystal structure allows for the displacement of ions, hence giving rise to the spontaneous polarization in the material [22]. Due to the different polarization directions of the ferroelectric and the screening lengths of the metal, two separate resistance states can be produced by affecting the band structure of the device. The physical parameter that is needed in our model in order to model the ferroelectric properties and calculate the bandstructure of the FTJ is the remanent polarization of the device. The

remanent polarization is found from literature where similar devices as the ones being modelled have been studied and is in the range 15-17 $\mu C/cm^2$ [24]. The polarization state pointing from the BE towards the TE is defined as the positive polarization state in our model and the opposite is the negative state.

Another constant that is needed in the calculation of the bandstructure of the device is the relative dielectric constant of the HZO. The relative dielectric constant is related to the polarization by conveying information on how easily the material is polarized when a electric field is applied [23]. The relative dielectric constant is found to be 25 [10].

2.3.2 Electron affinity and band gap

The electron affinity of a material is defined as the energy required to remove one electron from the bottom of the conduction band to the vacuum level [26]. The electron affinity plays a similar role as the workfunction of the metals, where the difference between the two gives the barrier height at the interfaces without considering polarization and bias. The affinity was calculated based on the work of Peng et al. by looking at the conduction band offset between silicon and HZO and so estimating the electron affinity to be 2.37 eV [27].

In our model, the calculation of the tunneling current is calculated with the WKB-approximation, the details will be covered in later sections. In the calculation of the transmission coefficient the decay constant (κ) needs to be estimated for each energy level within the band gap of HZO. The decay constant can be understood as the imaginary wave vector resulting from electronic states with energy below the conduction band edge, which in the effective mass approximation would lead to the following expression [26]

$$i\kappa = \frac{\sqrt{2m^*(E - E_C)}}{\hbar^2}, \;\; E < E_C \tag{2.12}$$

where m^* is the effective mass of the ferroelectric, E_C is the conduction band and E the energy. The effective mass approximation is, however, inaccurate for states far away from the conduction band and valence band edges, and instead k·p or density functional theory approaches have to be used. The way the decay constant is calculated is by constructing a function which interpolates values for κ from Dong et. al. [28] using a maximum value for κ and the band gap of the HZO to scale the values. The way the values are mapped can be seen in figure 2.4. The red line in figure 2.4 is the complex band structure of the HZO that the function is fitted to, where the highest energy value corresponds to the top of the barrier. The difference between the two points where κ_z, the

decay constant in the figure, is 0 is fitted to the band gap of the HZO. Using this together with the largest κ_z value for the red line, an interpolation in order to obtain a function for κ was done. The maximum κ value was taken to be approximately $4 \cdot 10^9\ m^{-1}$ in line with the results of Dong et al [28].

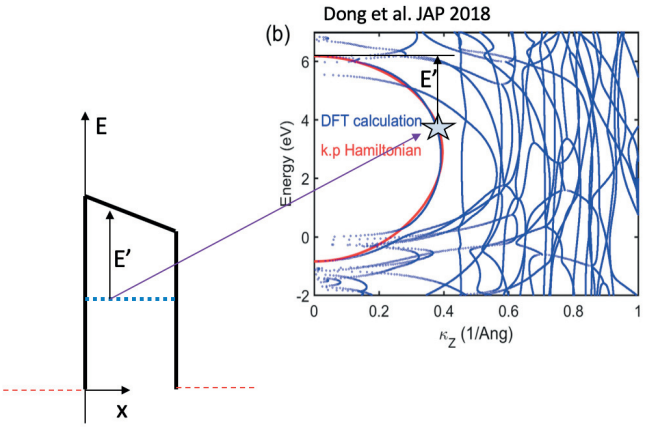

Figure 2.4: Diagram displaying how the energies in the band gap map to the to the values of the decay constant. Image adapted from Dong et al. [28].

2.3.3 Summary of parameters

The physical parameters needed to model the HZO are presented in table 2.2.

Table 2.2: Summary of the physical constants in the HZO

Affinity (eV)	**Relative permittivity**	**maximum κ m($^{-1}$)**	**Band gap (eV)**	**Polarization ($\mu C/cm^2$)**
2.37	25	$4 \cdot 10^9$	5.3	15

2.4 Band diagram of the FTJ

The modelling of the tunneling barrier of the FTJ is, as mentioned before, crucial in order to be able to calculate the current accurately. The approach and method to calculate the band diagram is based on the work of Pantel and Alexe [16]. The polarization of the ferroelectric layer and screening effects in the metals have a substantial impact on the bandstructure of the FTJ device and are in fact what enables the different resistance states of the device.

The polarization of the ferroelectric creates a surface charge on the interface between the ferroelectric and the metals that is equal to the polarization and will be labelled P_q [16]. The surface charge P_q is screened by the charge carriers within the metal, however imperfectly due to the screening length of the metals. The imperfect screening of the charges in the ferroelectric gives rise to a depolarization field going in the opposite direction of the polarization direction [32]. The asymmetry of the screening capability of the different metals leads to different barrier heights and band structures [16]. The change in barrier height due to the polarization is given by [16]

$$\Delta\Phi_i = \frac{l_i Q_s}{\varepsilon_0 \varepsilon_i} q, \quad i = 1, 2 \tag{2.13}$$

where ε_0 is the permittivity of free space, ε_i is the relative permittivity of the metal on the on the interface. The *i* is a index to label the metals in our case BE is 1 and TE is 2. l_i are the screening length of the metals that were calculated from Thomas-Fermi screening (see section 2.2.2) [16]. The screening charge density in equation 2.13 is labelled Q_s is given by

$$Q_s = \frac{P_q d}{\varepsilon_{HZO}\left(\frac{l_1}{\varepsilon_1} + \frac{l_2}{\varepsilon_2}\right) + d} \tag{2.14}$$

where d is the thickness of the ferroelectric film and ε_{HZO} is the dielectric constant of the HZO. The heights of the potential barrier at the interfaces are then given by [16]

$$\Phi_{L,R} = \Phi_i \pm \Delta\Phi_i \tag{2.15}$$

where *L* and *R* stand for the left and right interface respectively and are oriented as in figure 2.1. Φ_i is the barrier height without the polarization which is calculated by

$$\Phi_i = \phi_i - \chi \tag{2.16}$$

where ϕ_i is the workfunction of the metals and χ the electron affinity of the HZO. The plus sign in equation 2.15 is for the interface between TiN and HZO and the minus sign for W and HZO [16].

The way the polarization impacts the barrier height, according to the model used, could be understood from figure 2.5, where $\Delta\Phi_i$ and $\Phi_{L,R}$ are shown. In the figure the polarization of the ferroelectric is in the positive direction, giving negative charges on the left interface and positive

charges on the right interface, in the ferroelectric. These charges are screened in the metal, as shown in figure 2.3, and the opposite sign charges will accumulate on the interface in the metal. The accumulation of positive charges in the metal on the left interface leads to the conduction band bending upwards. Hence, increasing the left barrier height Φ_L by $\Delta\Phi_1$, given in equation 2.13. A similar effect takes place on the right interface, but the negative charges in the metal cause the conduction band to bend downwards, thus decreasing the right barrier height Φ_R by $\Delta\Phi_2$ given in equation 2.13.

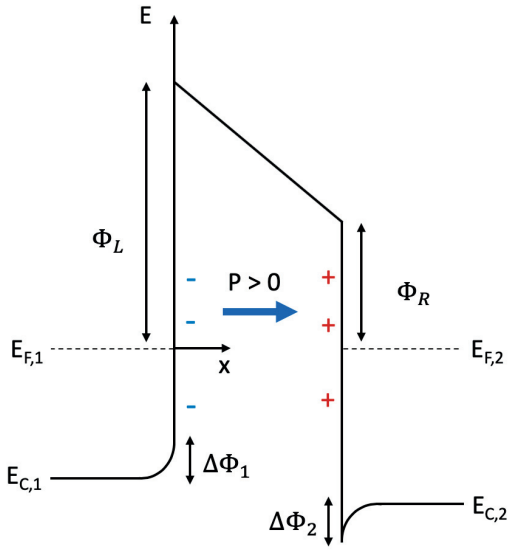

Figure 2.5: Band diagram displaying the change in barrier height due to polarization.

2.5 Current transport in FTJ

The current transport in FTJs is composed of four major conduction mechanisms. The four conduction mechanisms are direct tunneling (DT), Fowler-Nordheim tunneling (FNT), thermionic injection (TI) and trap-assisted tunneling (TAT). The direct tunneling is the quantum mechanical phenomenon where a particle has a possibility of transmission through a potential barrier [29], see figure 2.6. In the case of an FTJ the barrier is the ferroelectric material between the metal plates that will be tunneled through. Fowler-Nordheim tunneling is similar to direct tunneling in that they both are the same physical phenomenon. FNT, however, is tunneling through a reduced width of the barrier i.e tunneling through the triangular part of a barrier which could be seen in figure 2.6 [30]. Hence this current mechanism dominates at high voltages at which the barrier be-

comes mostly triangular in shape [16]. Thermionic injection occurs when an electron has sufficient thermal energy to overcome the potential barrier [17].

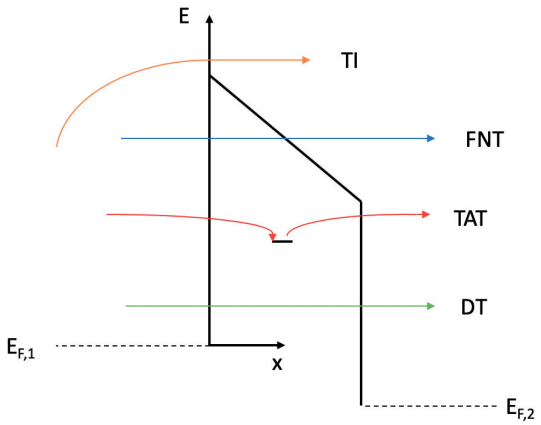

Figure 2.6: Band diagram (not to scale) displaying the different conduction mechanisms in an FTJ.

The last charge carrier mechanism that contributes to the current through an FTJ is trap-assisted tunneling. TAT, as the name suggests, is current transport through the barrier by the help of traps in the ferroelectric layer such as oxide vacancies or other defects in the ferroelectric [31]. The traps provide available energy levels within the band gap of the ferroelectric. As shown in figure 2.6 the electrons tunnel from the left metal contact into the trap and then tunnel out to the right metal contact. TAT allows for higher transmissions probability since the distance which the electron has to tunnel is shorter and the tunnel transmission probability decreases exponentially with the distance [29]. DT, FNT and TI are usually considered the three basic current mechanisms in FTJs but usually the current is dominated by either TAT or Poole-Frenkel emission, which is another type of trap-assited conduction mechanism, at higher voltages [24]. Research on similar devices as our modelled FTJ have concluded that TAT is the mechanism responsible for the current transport at voltages $|V| > 0.1V$ [10].

2.6 Model for transmission current

The model handling current due to direct tunneling, FNT and thermionic emission is inspired by the Tsu-Esaki model. These three current mechanisms will be labelled as the transmission current. The Tsu-Esaki model is a method by which one could calculate the tunneling current through one or multiple barriers by considering the Fermi-Dirac distribution, transmission coefficients, velocities of the electrons in material surrounding the barrier being tunneled through [33]. The model that is used in the simulations is more of a semiclassical model. The integral that is used to model the transmission current density going from right to left is displayed below

$$J_R = q \int_{E_C}^{\infty} v(E) f_0(E, E_{F1})(1 - f_0(E, E_{F2}))T(E)g(E)dE \tag{2.17}$$

The integration interval for the energy is from the band bottom of the metal to infinity in terms of energy. The q in front of the integral is the electron charge that turns the value from the integral into an electrical current [26]. The minus sign is left out as the current conventionally travels in the opposite direction. f_0 is the Fermi-Dirac distribution which gives the probability of a state being occupied at a certain energy level relative to the Fermi energy E_F at a given temperature. It is written as

$$f_0(E, E_{F,i}) = \frac{1}{1 + e^{(E - E_{F,i})/kT}} \tag{2.18}$$

where T is the temperature and k is Boltzmann's constant. The number index of the Fermi energy are the same as for the bandstructure calculations. The function $v(E)$ is the group velocity of the electrons at certain energy levels relative to the band bottom in the metal which is implemented in the model of the metal and is given by the equation below [6]

$$v(E) = \frac{1}{\hbar}\frac{\delta E}{\delta k} = \frac{\hbar k(E)}{m^*} \tag{2.19}$$

where m^* is the effective mass and k is the wavenumber. The wave vector as a function of energy is given by [6]

$$k(E) = \frac{\sqrt{2m^* E}}{\hbar} \tag{2.20}$$

where the energy E is measured from the band bottom in the metal. The $g(E)$ factor is the three dimensional density of states for the metal relative to the band bottom, similarly to the velocity implemented in the metal model and is given by [6]

$$g(E) = \frac{(2m^*)^{3/2}}{2\pi^2\hbar^3}\sqrt{E} \tag{2.21}$$

where the energy is measured from the band bottom of the metals. The density of states together with f_0 gives the number of electrons that are available for tunneling. The factor $1 - f_0(E, E_{F2})$ is the probability of a state being unoccupied in the metal on the left side (W in the FTJ model) which is needed in order to determine whether electrons that can tunnel through are able to find a state to occupy. Only half of the density of states are also considered in the integral since only positive k-values will travel in the direction of the barrier and thus contribute to the current in the case of electrons travelling from BE to TE [26].

In the model used, the velocity and the density of states are put to the minimum value of the two metals in both current directions. The reason for this is that, there is a non-zero current at 0 V without setting them to the minimum value. When the minimum values are used, the current will be zero for 0 V, due to the occupational probabilities being equal. The non-zero current at 0 V occurs because a semiclassical model is used, which is not strictly derived based on quantum mechanics like the Tsu-Esaki model. When following the Tsu-Esaki model, the integration over energy will account for the states in the longitudinal direction i.e. the *x*-direction. The density of states will hence only be needed for the *y*- and *z*-components. This is not considered in our model, causing the issues with the unbalanced current at 0 V.

The $T(E)$ factor in the current density integral is the transmission coefficient which describes the probability that an electron will tunnel through the barrier. The transmission coefficient is calculated with the help of the Wentzel-Kramers-Brillouin (WKB) approximation. The WKB-approximation is a theory which solves the Schrödinger equation for a system which has slowly varying potential in the spatial direction [26]. The solution to the Schrödinger equation with a non-varying potential consists of plane waves of the form $exp(ikx)$ [29]. With a varying potential the product *kx* is turned into an integral to account for the variation in potential and so the wavenumber. From this basis solutions to the Schrödinger equation can be deduced which are known as WKB-approximations [26]. The WKB-approximation for tunneling through a barrier is given by

$$T(E) = exp\left(-2\int_{x_L(E)}^{x_R(E)} \kappa(E'(x))dx\right) \tag{2.22}$$

where $x_R(E)$ and $x_L(E)$ are the *x*-positions of the right and left side of the potential barrier which could vary depending on the energy if the integration is done for the triangular part of the potential barrier. The approximation integrates over the decay constant κ which in our model is a function which depends on the energy gap to the conduction band of the HZO as displayed in figure 2.4. This energy gap is then dependent on the *x*-position within the barrier.

Similarly the left going current is calculated but with the right parameters and constants for the top electrode. The total current density is hence given by

$$J = J_R - J_L \tag{2.23}$$

2.7 Models for the TAT current

In the simulations of the current transport two models were used in order to try to model the TAT current.

2.7.1 Initial model

The initial model for the TAT current was based on the work of Cheng et al. [34] but modified with slightly different assumptions. The basic concept of how the model was implemented could be understood from figure 2.7. The model in its simplest form assumes a single trap state due to some material defect located at energy E_t below the conduction band of the ferroelectric. In the presence of a trap state electrons have the possibility of tunneling into the a trap from the cathode (orange point in figure 2.7) and then tunnel out from the trap state into the anode.

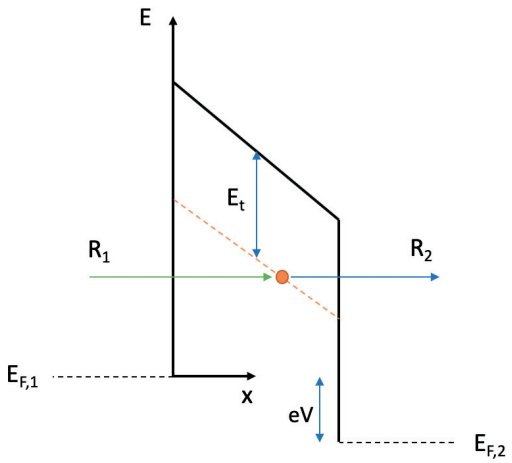

Figure 2.7: Schematic energy band diagram of the tunneling rates involved in TAT model.

In order to model the current two tunneling rates are introduced R_1 and R_2 [34]. The R_1 is the tunneling rate for entering the trap and R_2 for tunneling out of the trap. The rates are expressed as [34][31].

$$R_1 = \nu_0 N_t f_0(E, E_{F1}) T_1 \tag{2.24}$$

$$R_2 = \nu_0 N_t (1 - f_0(E, E_{F2})) T_2 \tag{2.25}$$

where N_t is the trap concentration, ν_0 could be described as the frequency at which electrons"attempt" to tunnel through to the trap, f_0 is the Fermi-Dirac distribution given by equation 2.18 and $T_{1,2}$ are the transmission probabilities calculated with equation 2.22. By assuming that the rate of change of electron concentration in the traps is constant one could deduce that the tunneling for a trap is

$$R_t = \left(\frac{1}{R_1} + \frac{1}{R_2} \right)^{-1} = \frac{\nu_0 N_t f_1 (1 - f_2) T_1 T_2}{f_1 T_1 + (1 - f_2) T_2} \tag{2.26}$$

where f_1 and f_2 are the Fermi-Dirac distributions of TE and BE respectively. A single trap could

be considered a small interval *dx* by which a little portion of the total current is passing through. The TAT current density in one direction is then expressed as

$$J_{TAT} = \int_0^d q \left(\frac{1}{R_1} + \frac{1}{R_2} \right)^{-1} dx \tag{2.27}$$

where d is the thickness of the ferroelectric. It should be noted that the interface between BE and HZO is considered $x = 0$ and the interface between TE and HZO is $x = d$. In Cheng et.al [34] it is assumed that there is no occupancy in the anode, thus meaning that there is only current going in the right direction if we consider the case of figure 2.7 where a positive voltage is applied to the top electrode. However this was deemed an unreasonable assumption so the model used considers TAT current density in both directions as in the transmission current model.

2.7.2 Second model

The second model of the TAT current that was used in simulation was based of the work of Jimenez-Molinos et al. [35]. The approach in this method of calculating the TAT current is fundamentally more quantum mechanical than the initial model. In this model the current in the opposite direction is disregarded. This model also uses two rates in order to model the current through a trap but how the rates are expressed differ. As in the previous model, by assuming that the rate of change of the concentration of occupied traps is constant, the number of transitions per unit time by traps at a certain energy E and position *x* is

$$R(x, E) = \frac{N_T(x, E)}{\tau_c(x, E) + \tau_e(x, E)} \tag{2.28}$$

where $N_T(x, E)$ is the trap concentration at energy E and position *x*, $\tau_c(x, E)$ and $\tau_e(x, E)$ are the time constants of capture and emission respectively [35]. The total current density is from this expressed by

$$J_T = q \int_0^d dx \int_{E_C}^{\infty} \frac{N_T(x, E)}{\tau_c(x, E) + \tau_e(x, E)} dE \tag{2.29}$$

where q is the electron charge and d the thickness of the ferroelectric film. As one could see from equation 2.29 $N_T(x, E)$, $\tau_c(x, E)$ and $\tau_e(x, E)$ are all dependent on the position and energy, but we will assume initially that $N_T(x, E)$ is a constant of the energy and *x*-positions where traps

are found. Here we assume a single trap energy level as displayed in figure 2.7. The time constants in our model, simplified from Jimenez-Molinos et al.[35], are computed by the following expressions

$$\tau_c^{-1}(x,E) = \int_{E_C}^{E} g_c(E) f_c(E, E_{F1}) W_c(x,E) dE \tag{2.30}$$

$$\tau_e^{-1}(x,E) = \int_{E_C}^{E} g_a(E)(1 - f_a(E, E_{F2})) W_e(x,E) dE \tag{2.31}$$

The c and a indicate whether it is the cathode or anode respectively. The $f_c(E)$ and $f_a(E)$ are the Fermi-Dirac distributions of the cathode and anode respectively. The $g_{c,a}$ are the density of states given for the cathode/anode given by equation 2.21. $W_{c,e}(x,E)$ are the probabilities of capture or emission of an electron per unit time by the trap [35]. In order to calculate $W_{c,e}(x,E)$ Fermi's golden rule is utilized [36]. Fermi's golden rule in simple terms could be described as the probability of transition between two states per unit time [37]. Hence $W_{c,e}(x,E)$ is given by [35]

$$W_{c,e}(x,E) = \frac{2\pi}{\hbar} |\langle f|H|i\rangle|^2 \delta(E - E_t) \tag{2.32}$$

where $|i\rangle$ is the initial state in the metal and $|f\rangle$ is the final trapped state in case for capture and the reverse applies for emission, $\hbar$ is the reduced planck's constant. The scalar product of the states $\langle f|H|i\rangle$ is given by the integral

$$\langle f|H|i\rangle = \int \Psi_f^*(\mathbf{r}) H(\mathbf{r}) \Psi_i(\mathbf{r}) d\mathbf{r} \tag{2.33}$$

where Ψ_f and Ψ_i are the wave functions of the final and initial states respectively and H is the Hamiltonian of the trap region. The Hamiltonian is given by

$$H = \begin{cases} -E_t, & \text{if } x \in [x_0 - \frac{x_T}{2}, x_0 + \frac{x_T}{2}] \\ 0, & \text{if } x \notin [x_0 - \frac{x_T}{2}, x_0 + \frac{x_T}{2}]. \end{cases} \tag{2.34}$$

where E_t is the energy below the conduction band of the ferroelectric that the traps are located at, x_0 is the x-position of the center of the trap, and x_T is the side length of the trap. In the model it is assumed that the traps are a cubic box with volume V_T and side length x_T [35]. The side length according to Jimenez-Molinos et al. [35] is given by

$$x_T = \frac{\sqrt{\frac{4\pi}{3}\hbar}}{\sqrt{2m^* E_t}} \tag{2.35}$$

where m^* is the effective mass of the HZO. From equation 2.35 x_T was estimated to be approximately 1nm using $0.11m_0$ as the effective mass for HZO [39]. Compared to the 4.5 nm thickness of the HZO, the calculated x_T is large and will thus be used as a fitting parameter. In the work of Jimenez-Molinos et al. the wave functions of the final and initial states are three dimensional. However after some approximations equation 2.33 becomes an integral in one dimension. Therefore practically the simplified wave equation of the final state that we use is

$$\Psi_f(x) = \begin{cases} \frac{1}{\sqrt{x_T}}, & \text{if } |x - \frac{x}{2}| < \frac{x_T}{2} \\ 0, & \text{elsewhere.} \end{cases} \tag{2.36}$$

For the wave function of the initial state we use the WKB-approximation. The choice is motivated by the fact that we expect a exponentially decaying wave function inside the barrier. In order to be able to estimate the decay we use the WKB-approximation as we have a varying barrier potential. The wave function of the initial state is hence expressed by [26]

$$\Psi_i(x) = \frac{1}{\sqrt{\kappa(x)}} exp\left(-\int_0^x \kappa(x')dx'\right) \tag{2.37}$$

where κ is the decay factor which will in the simulations be calculated with the help of the κ function mentioned in previous sections. The factor $1/\kappa$ is needed in order to conserve current that would otherwise change due to the change in κ. Thus by inserting these wave functions and the Hamiltonian into equation 2.33 and then equation 2.32 on obtain the following expression for $W_{c,e}(x, E)$ for positions and energies where the traps are found

$$W_{c,e}(x, E) = \frac{2\pi}{\hbar} \left| \frac{E_t}{\sqrt{x_T}} \int_{x-\frac{x_T}{2}}^{x+\frac{x_T}{2}} \frac{1}{\sqrt{\kappa(x)}} exp\left(-\int_0^x \kappa(x')dx'\right)\, dx \right|^2 \tag{2.38}$$

Depending on whether the emission is from BE or TE the integration of κ will be done from either 0 to *x* or from *x* to d respectively.

Chapter 3

Methodology

The tool that was used in order to implement the models presented above was MATLAB. The initial models and simulation tools were provided by my supervisor to be improved and add to it a model of the TAT current. Throughout the project small changes were done in order to try to improve the model and the code but the general structure was kept the same.

3.1 Work process

The work process of this thesis could be divided into three stages. The first one involved an evaluation of the initial TAT current model and investigation on how it could be improved. After evaluation a decision was made to move on to look for new models to test. In the second stage a new model was implemented and continuously improved. The third stage involved trying to optimize the improved models and analyze the findings.

3.2 Structure of the code

In general the simulation code is categorized into three different parts the classes describing the material parameters, functions which perform the necessary calculations and a fitting tool. The materials are modeled by creating classes which contain all the necessary parameters and functions which are related to the properties of the metal electrodes or ferroelectric. The input parameters, calculated parameters and functions are summarized in table 3.1. These models were used to extract the necessary parameters and constants for the calculations of the current density.

Table 3.1: Overview of the material classes used in simulation.

Class (Material)	Metal	Ferroelectric
Input Parameters	Workfunction (eV) effective mass Electron density (m^{-3})	Affinity (eV) thickness (m) Band gap (eV) Relative dielectric constant Maximum κ Polarization (C/m^2)
Calculated parameters	Fermi energy (eV) (eq. 2.5) Screening length (m^{-1}) (eq. 2.9)	
Functions	Density of states ($m^{-3}J^{-1}$) (eq. 2.21) Velocity (m/s) (eq. 2.19) Effective dielectric constant (eq.2.8)	Calculate $\kappa(x)$ Flip polarization

The structure of the code and how the different parts of it are connected to each other could be visualized in figure 3.1. The main script for performing simulations is *FitFTJ_metapod* where the model is simulated and then optionally fitted to experimental data. The tool used to perform the fitting is MATLABs nonlinear least-squares solver. In order to be able to perform the fitting a function which is used to update the parameters during fitting is needed which is satisfied by *Jvfitfunc*.

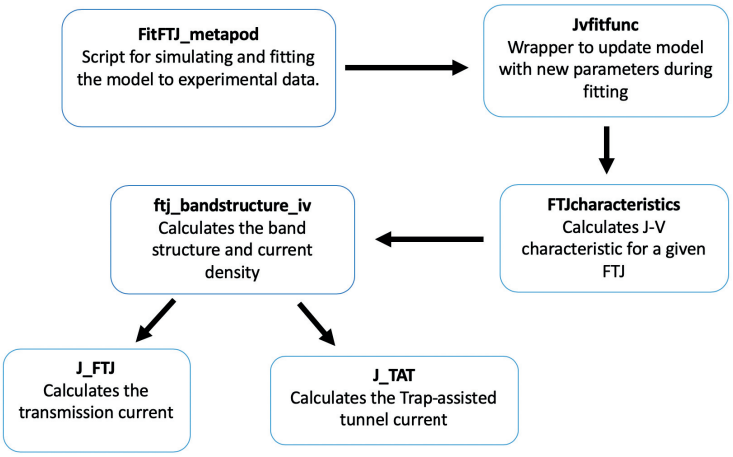

Figure 3.1: Schematic of the code structure.

This function then utilizes the function *FTJcharacteristics* which calculates the current density for both polarization directions. The way it does this is by using another function, *ftj_bandstructure_iv*. This function calculates the band structure using equation 2.15 and the current density by using the two functions *J_FTJ* and *J_TAT*. The function *J_FTJ* implements the transmission current model described in section 2.7 and calculates current density that is a consequence of direct tunneling, Fowler-Nordheim tunneling and thermionic emission. The model of the TAT is implemented in the function *J_TAT* and similarly to the transmission current function aims to calculate the current density but due to the TAT current mechanism.

3.3 Implementation of TAT-model

The implementation and testing of the second model was the main work of this project. In order to implement equations 2.29,2.30,2.31 and 2.38, which govern the current flow, in an effective manner a separate function for $W_{c,e}(x, E)$ was defined that later is utilized in the main TAT code. The implementation of $W_{c,e}(x, E)$ made it simpler to deal with the separate integration intervals. The main issue with implementing the model is how to compute the integrals of the equations in question.

In order to calculate the integrals in the equations a combination of loops and MATLAB's numerical integration function were applied. MATLAB's numerical integration function was applied for the integral in the wave function of the initial state found in equation 2.37 and the time constants. The remaining integrals were calculated using a summation by the help of a for-loop which looped over the equations and then summed the values up. When using loops to numerically evaluate an integral one needs to divide the integration interval into a certain number of subintervals for which the function being integrated is evaluated. The accuracy of this method is evidently dependent on how fine the subintervals are divided. In order to save time during simulations the number of loops were limited to maximum of 50 which likewise is the number of subintervals. For the 4.5nm thickness of the device this would result in trap intervals of $dx = 90$ pm which is small compared to Yu et al. where 0.3-0.6 nm is the estimated distance between traps [31], suggesting it is slightly unreasonable. This value would overestimate the number of traps and so possibly resulting in increased current values. The size of the energy subinterval is estimated based on the number of traps.

Chapter 4

Results and Discussion

In this section the results from the simulations of the models will be presented in order to display how well we managed to get them to correspond to experimental data. The analysis will mainly be focused on evaluating the TAT current models and not as much on the accuracy of the transmission current as this with some parameter changes was deemed sufficiently well fitted. All data was simulated for 300K as the temperature and for a voltage range between -0.5 V to 0.5 V unless anything is stated. Furthermore, experimental I-V curves with polarization pointing in either up or down direction were used in the fitting.

4.1 Comment on experimental data

In the evaluation of the TAT models and how well they match experimental data, two different data sets are used. In the first model the experimental data happened to contain a tungsten oxide (WO_x) layer between the W and HZO which affects the current levels and renders the model inaccurate. For the second model however a new data set is used which is supposed to be pure metal contacts and HZO interfaces. It should also be noted that the thicknesses of the ferroelectric film in the two are different, 5 nm in old data and 4.5 nm in new data.

4.2 Evaluation of the initial TAT-model

In the first simulations the initial parameters presented in tables 2.1 and 2.2 (with 5 nm thickness). The initial simulations were performed without the TAT current as it was expected to be give poor results.

The results of the first simulations with the parameters in tables 2.1 and 2.2 are displayed in figures 4.1a and 4.1b. The curves plotted in figure 4.1a are done without the TAT current. In figure 4.1a the current density as a function of the voltage is displayed. The dotted lines are the values calculated by the simulation and the full lines are the experimental data. The red colored data is for positive polarization and the blue for negative polarization. What could be observed is that the initial parameters inserted do not match well with experimental data as the current calculated is too small. There could be several reasons for this e.g. inaccurate parameters, faulty bandstructure that affects the data.

In figure 4.1b the calculated bandstructure for 0 V is displayed, from the heights of the barrier we could conclude that the heights are within reasonable intervals for the two polarizations [20]. The blue barrier is for the positive polarization direction and the orange line for negative polarization. One could observe that the barrier height is larger for $P < 0$ which is why the current for the negative polarization state is smaller. The difference in current levels of the two polarization states in figure 4.1b suggests that the parameters and equations responsible for the calculation of the barrier heights do have some validity and correspondence to the physical behaviour of the FTJ.

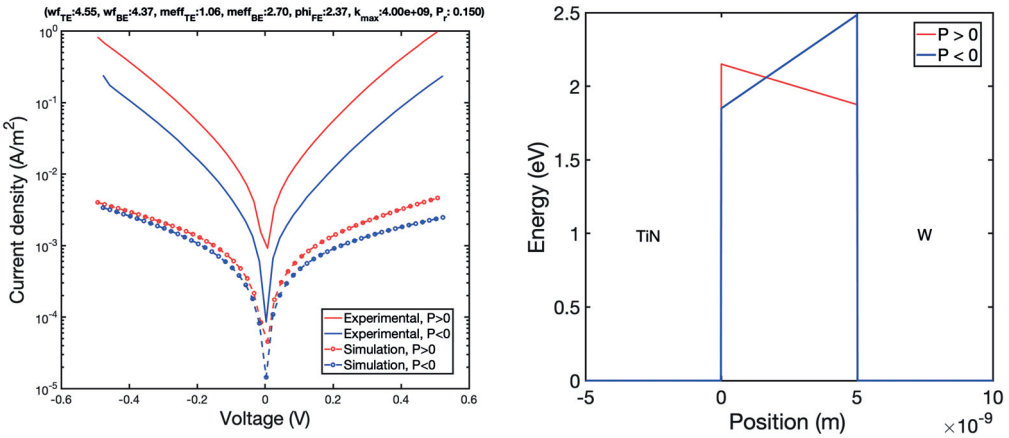

(a) J-V plot for model and experimental data. **(b)**

Figure 4.1: First simulation of initial parameters without TAT current. (a) J-V (current density-voltage) plot for model and experimental data. (b) Band diagram for 0 V.

After attempts of fitting some of the parameters a decent fit was achieved by decreasing maximum κ value to $\kappa_{max} = 3.7 \cdot 10^9\ m^{-1}$ and with all the other parameters kept constant. The new fit is

presented in figure 4.2 where the current density as a function of the bias over the FTJ is plotted. The decrease in κ_{max} lead to a significant impact in the current levels in the simulation. This is due to that the transmission probability, equation 2.22, is negatively exponentially dependent on κ meaning that the impact of changing κ is large. In figure 4.2 the fit for $P > 0$ is very good for lower biases. The same could not be said for $P < 0$ which probably is due to the bandstructure model used. For both polarization states the current density computed by the transmission current model is too low at higher voltages. For higher bias levels the TAT current transport mechanism is expected to dominate [24] thus the TAT model is introduced to address the issue.

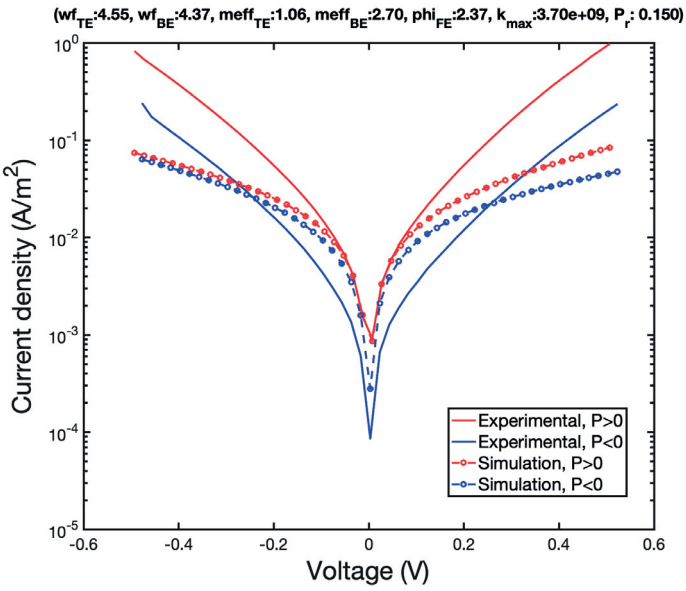

Figure 4.2: J-V plot of the transmission current with $\kappa_{max} = 3.7 \cdot 10^9\ m^{-1}$ and experimental data.

The current density as a function of the voltage applied with the transmission and TAT current both included in the simulation is shown in figure 4.3a. The same input parameters were used. The same type of plot with only the TAT current considered could be seen in figure 4.3b. The parameters that were chosen for the TAT model were $E_t = 1.82$eV and $\nu_0 = 10^{13}$Hz [31][38]. For the trap concentration the value was set to be $N_t = 10^{25}$m^{-3}[40]. All of the mentioned parameters are used as fitting parameters within reasonable intervals. By altering these parameters the best fit was achieved with $E_t = 1.82$ eV, $N_t = 10^{24}$ m^{-3} and $\nu_0 = 10^{12}$ Hz and is shown in figures 4.3c and 4.3c. The magnitude of the current in this fit matches the experimental data well but the main issue is that the current is non-zero at 0V since it is expected to be zero when no bias is applied.

The J-V dependence for the simulated data agrees somewhat with the experimental data for $P > 0$ but less so for $P < 0$. Simulations with current going only in one direction were also carried out but the results were unsatisfactory and were not included since they provide no further insights or improvements in understanding the TAT model.

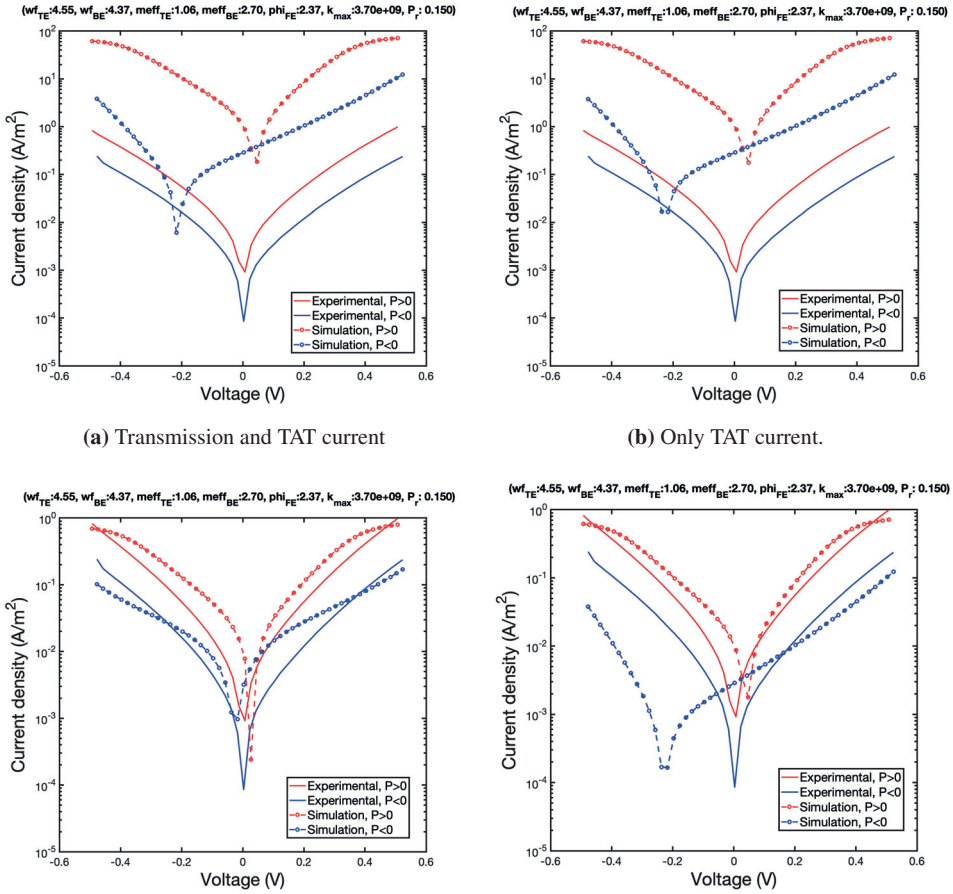

(a) Transmission and TAT current

(b) Only TAT current.

(c) Transmission and TAT current.

(d) Only TAT current.

Figure 4.3: Figures (a) and (b) display J-V curves for FTJ simulations of transmission and TAT currents with $E_t = 1.82$ eV, $N_t = 10^{25}$ m^{-3} and $\nu_0 = 10^{13}$ Hz. Figures (c) and (d) display J-V curves for FTJ simulations of transmission and TAT currents with $E_t = 1.82$ eV, $N_t = 10^{24}$ m^{-3} and $\nu_0 = 10^{12}$ Hz.

In order to asses the cause of the non-zero current at 0V the tunneling rates, equations 2.24 and

2.25, and the bandstructure of the simulation model were assessed. This was done by simulating the current for barriers with varying height differences ($\Delta\phi$) for the left and right barrier at 0V. It showed that greater $\Delta\phi$ resulted in larger negative current which could be seen in figure 4.4a. Studying the band diagram displayed in figure 4.4b one observes as the inclination increases the gap between the trap-state and Fermi energy of TE decreases. This results in greater negative current (going from W to TiN) which indicates that the Fermi-Dirac distribution found in the rate equation is a decisive factor.

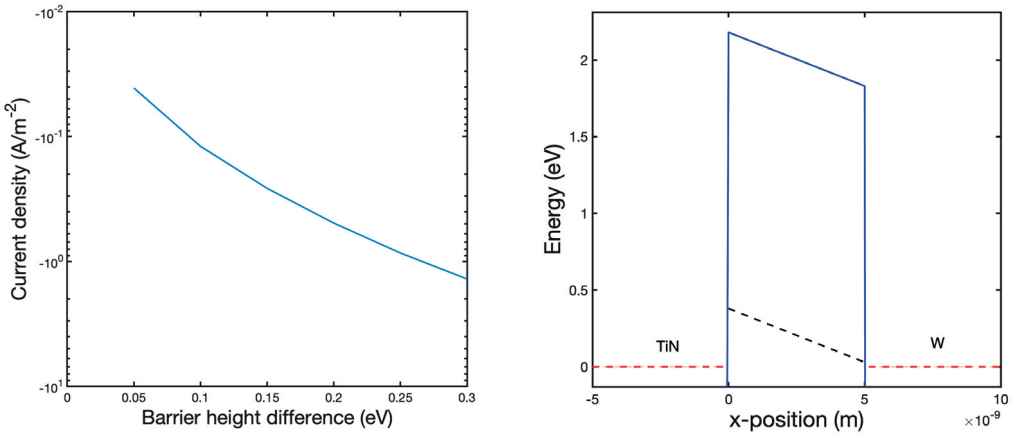

Figure 4.4: (a) J as a function of barrier height difference between BE and TE. (b) Band diagram for $\Delta\phi = 0.3$ eV with the trap state and Fermi level represented by the grey and red dashed lines respectively.

This is confirmed by viewing how parameters included in the equations for the transmission rates R_1 and R_2 behave for two separate $\Delta\phi$. In figures 4.5(a)-(e) and 4.6(a)-(e) such parameters for $\Delta\phi = 0.05$ eV and $\Delta\phi = 0.3$ eV respectively are displayed. When the gap between the Fermi level and the trap state closes when going from $\Delta\phi = 0.05$ eV to 0.3 eV, see figures 4.5a and 4.6a, the probability of a state being occupied by an electron at the level of the trap state increases. Furthermore due to the exponential nature of the Fermi-Dirac distribution (equation 2.18) the probability of finding an unoccupied state to tunnel to is close to one for all energies above E_F. This is evident in figures 4.5b and 4.6b where the probability of a state being occupied in BE and unoccupied in TE for the energy interval at which the trap states are found is displayed. Since the transmission probabilities for the same tunneling distance never differ more than a factor 10 for equal tunneling

distances for both $\Delta\phi$ values, see figures 4.5c and 4.6c, the R_1 rate will be the decisive term in the expression of the total rate in equation 2.26. Thus the difference between the R_1 of the right going and left going currents is going to increase with larger $\Delta\phi$ but R_2 for the two current directions remain unchanged which is verified in figures 4.5d, 4.5e, 4.6d and 4.6e.

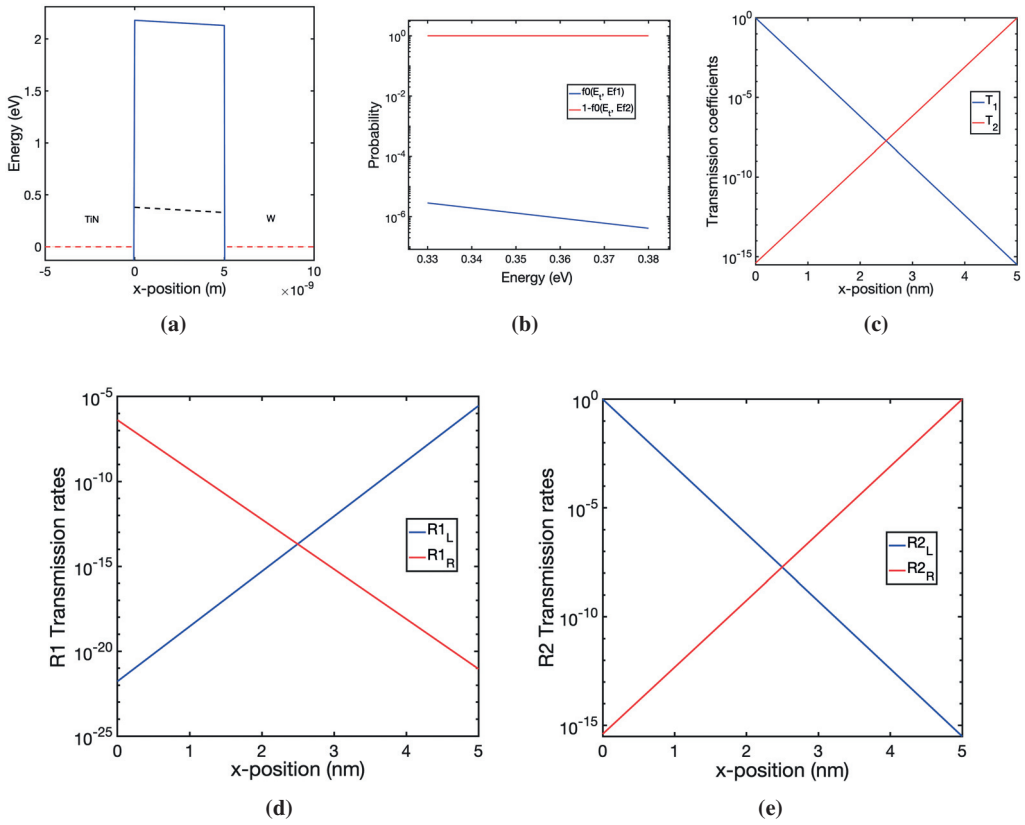

Figure 4.5: Plots of rate equations and important parameters for (equations 2.24 and 2.25) for $\Delta\phi = 0.05$ eV at 0 V. (a) Energy band diagram. (b) Probability of occupation and free states for electrons in current going in the right direction. (d) R_1 for current in both directions. (e) R_2 for current in both directions

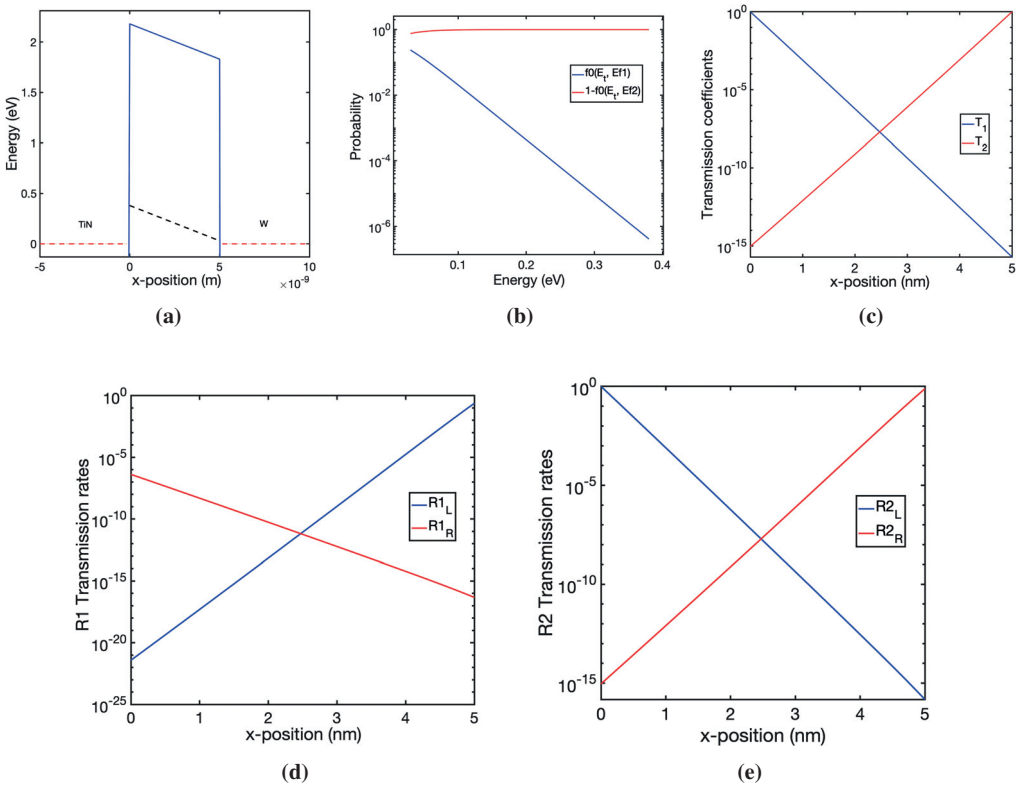

Figure 4.6: Plots of rate equations and important parameters for (2.24 and 2.25) for $\Delta\phi = 0.30$ eV at 0 V. (a) Energy band diagram. (b) Probability of occupation and free states for electrons in current going in the right direction. (d) R_1 for current in both directions. (e) R_2 for current in both directions.

From this realization and the fact that the model does not account for several possible physical parameters such as, the probability that a trap is occupied, the number of electrons available for tunneling etc. a decision was made to search for a model describing the rates in a more accurate manner. It should be noted that studies have successfully fitted data using similar models suggesting that some underlying assumption we use might be causing the deviating results [31]. This was not investigated further beyond this point as the search for new models began.

4.3 Implementation of second model and optimisation of the parameters

The implementation of the second model involved solving some errors in the implementation which caused trouble in obtaining reasonable results. However, in the final stage of implementation this was achieved and the results showed better resemblance to experimental data. The focus then shifted to optimisation of the parameters for bandstructure and trap states which are vital for the shape and magnitude of the simulated current.

From now on the simulation data was compared and fitted to new experimental data where the thickness of the HZO was 4.5 nm. The parameters from tables 2.1 and 2.2 were used except $\kappa_{max} = 3.7 \cdot 10^9\ m^{-1}$. The results are shown in figures 4.7a and 4.7b. The depth of the trap energy level was simulated for $E_t = 1.77$ eV as this value was extracted by Athle et al.[24] for the same devices and $x_T = 0.1$ nm. Studying figure 4.7a one could see that the J-V dependence is improved and seems to match the slope of the experimental data. The current magnitude is much too low and the gap between the current for $P > 0$ and $P < 0$ is too wide for negative biases. The large difference in current could be understood from the band diagrams in figures 4.7c and 4.7d, where in the case of $P < 0$ the trap level is located higher relative to the Fermi level than for $P > 0$ in W. Thus due to the Fermi-Dirac distribution decreasing exponentially the further from the Fermi level the electron is located, the current decreases as τ_c is increased.

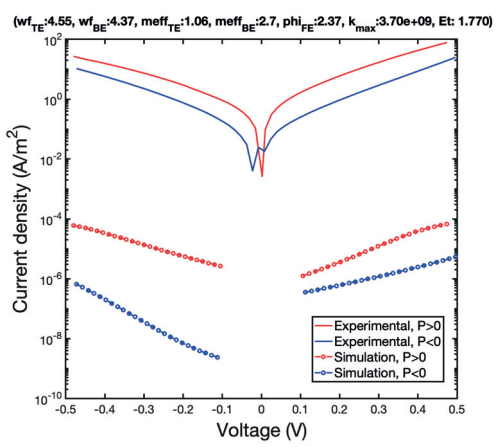

(a) $N_t = 10^{25}\mathrm{m}^{-3}$.

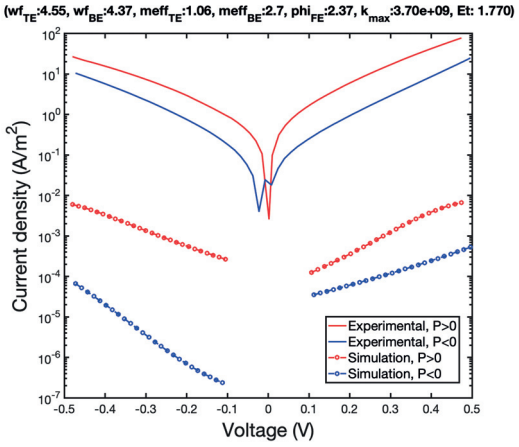

(b) $N_t = 10^{27}\mathrm{m}^{-3}$.

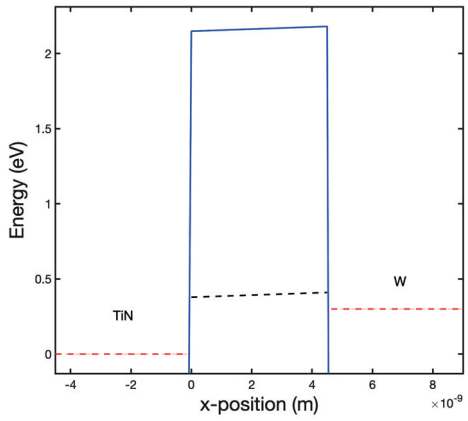

(c) $P > 0$

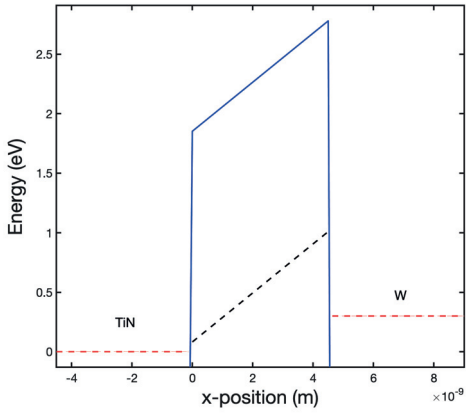

(d) P<0

Figure 4.7: (a)-(b) J-V curve for the simulated TAT current for different N_t. (c)-(d) Band diagram for -0.3V for both polarization directions.

In order to increase the magnitude of the current the first parameter that was changed was N_t. The effect of changing N_t was expected to be a linear increase in the current according to equation 2.29 which seen in figure 4.7b where was increased to $N_t = 10^{27}$ m^{-3}. The value for N_t is high compared to the oxygen density in HfO_2 being $3 \cdot 10^{28}$ m^{-3} but not unreasonable as such high defects have been modelled [41].

The other parameters that could be varied in order to affect the current are the workfunction of TiN

(ϕ_{TiN}), free electron densities of the metals, the trap side length x_T and the depth of the trap level E_t. Most of these parameters intricately affect how the current is altered. Therefore it is important to understand the way they affect the current and band structure to be able to provide suitable input parameters to the fitting function.

In order gain understanding for how the different parameters governing the TAT affect the current density one could study figure 4.8. In this case we have electrons being transmitted from the TiN to the W due to the voltage applied. In figure 4.8 plots for the different parameters are displayed for $V = 0.2$ V and $P > 0$. By studying figures 4.8d, 4.8e and 4.8f one could observe that the two main factors affecting the time constants are the Fermi-Dirac distribution and $W_{c,e}(x, E)$ due to their exponential dependence on the energy and tunneling distance respectively. The DOS varies more slowly with energy, but the magnitude is within the expected range. When a voltage is applied to TE, the slope of the trap energy level will change, resulting in large changes in the occupational probabilities for the trap level energies in the metals. Thus, the main factor affecting the current-voltage dependence is the Fermi-Dirac distribution seen in figure 4.8f, which decreases exponentially when $E - E_{F,i}$ increases, where E is the energy of an electron. However, for large tunneling distances $W_{c,e}(x, E)$ decreases exponentially as expected. Meaning that in the case when the difference between the trap energy and Fermi level is small as in figure 4.8a the occupational probability in TiN will be high. This would result in a high current, if not the $W_{c,e}(x, E)$ term decreased so rapidly with distance. The exponential decrease with distance diminishes the effect of the Fermi-Dirac distribution and giving a smaller current for long tunneling distances. This is concluded to be an expected and physically reasonable behaviour by the equations modelling the transitions of the electrons. The interaction of the occupational probability and $W_{c,e}(x, E)$ will give a current peak for a certain distance into the HZO, as is seen in figure 4.8b, when the time constants reach a combined minimum value as in figure 4.8c. Hence, balance between the Fermi-Dirac distribution and $W_{c,e}(x, E)$ results in the current voltage dependence seen in the J-V plots.

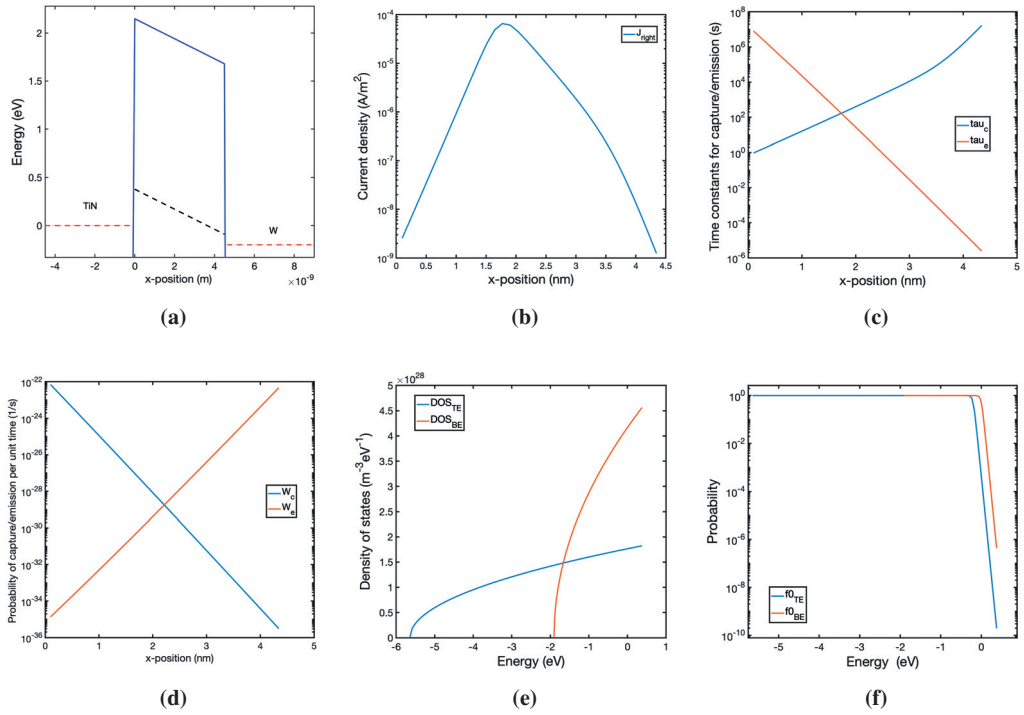

Figure 4.8: Simulation of parameters for $V = 0.2V$ and $P > 0$. (a) Band diagram. (b) Current density as a function of *x*-position. (c) Time constants for capture and emission as a function of *x*-position. (d) $W_{ce}(x, E)$ as a function of *x*-position. (e) Density of states as a function of energy. (f) Fermi-Dirac distribution as a function of energy.

The trap side length x_T was also studied to understand its effect on current through the FTJ. The trap side length x_T, similarly to N_t, has a linear effect in general on the current density, with some affect on the J-V dependence since it affects the size of $W_{c,e}(x, E)$. In figure 4.9a the current density has increased with approximately factor 10 compared to figure 4.7a but no effect on the shape of the plots is seen. This is due to that $W_{c,e}(x, E)$ has a linear increase with x_T as seen in figure 4.9b when the length is changed from 0.1 nm to 1 nm. Thus there is an increase in $W_{c,e}(x, E)$ and so the current. There is some affect on the shape of the current data, due to the relation explained in figure 4.8 but in general there is an linear increase unless the value of x_T is set to extreme values.

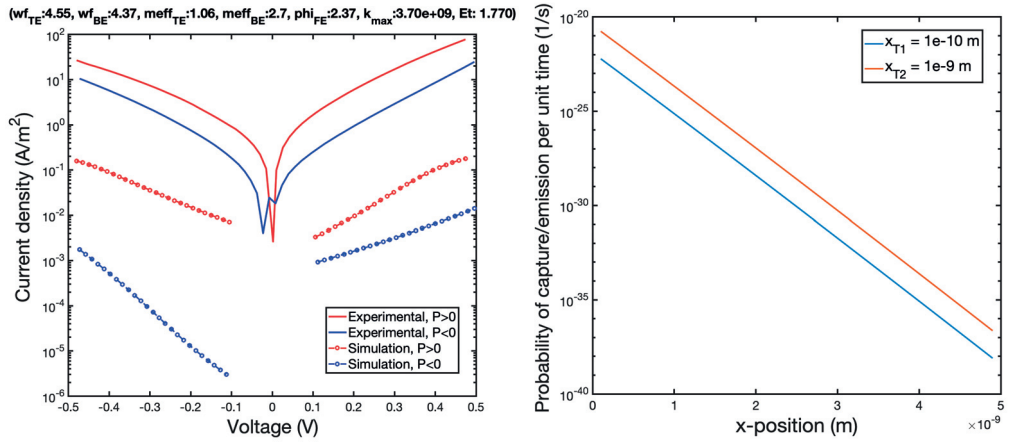

(a) **(b)**

Figure 4.9: (a) J-V plot of TAT current with $x_T = 1$ nm. (b) Plots for W_{ce} over x-position for $x_T = 0.1$ nm and $x_T = 1$ nm

Some automatic fitting was attempted for the free electron density but the values were never noticeably altered thus never lead to any improvement of the TAT fit. The free electron density affects the screening lengths and by that the effective dielectric constant which are important parameters in modulating the barrier heights of the FTJ (equation 2.14) and so the current. However it simultaneously affects the barrier heights at both interfaces for the metals and when changing the barrier height, E_t and x_T often need to be adjusted as well to make a good fit. Hence making it a complicated optimization problem to solve which probably is the reason the variable is not changed by the fitting function.

In order to minimize the current difference of the two polarization states and increase the magnitude the effects of changing ϕ_{TiN} and E_T were observed. The general results could be seen in 4.10. One could go into depth about why the individual results behave the way they do but this is uninteresting in terms of understanding the validity of the model. Some general trends could be observed such a saturation of the current at higher voltages in figures 4.10a, 4.10c and slightly in 4.10d. Furthermore there is no improvement of the difference in current for the negative voltages instead the J-V dependence is worsened for both biasing directions. Two conclusions could be drawn from the data. The first is the current level cannot be significantly increased by varying the bandstructure in order to increase transmission as it leads to other undesired effects in the simulation indicating that there is probably a normalization error involved which is the cause of the

small current levels. The normalization error could be due to simplification of the wave function compared to Jimenez-Molinos et al.[35] where device area is compared to the size of the trap as a normalization constant, which we in our model take no consideration of. An error in normalization will also affect the value of $W_{c,e}(x, E)$ which has an impact on the voltage dependence of the current as was seen in figure 4.8. This might have contributed to some of the effect regarding the J-V dependence. Other parameters could be too simplified such as the single trap level which also would diminish the TAT current simulated. The current could however be increased through parameters which have a linear effect on the current but not enough in order to obtain a good fit. The second conclusion is that the calculation of bandstructure is not complex enough to account for physical effects such as image force lowering of the barrier [35] or possibly piezoelectric effects [42], which is seen due to the inability to affect the gap for negative biases and the worsening of the J-V dependence compared to experimental data when the parameters are modified.

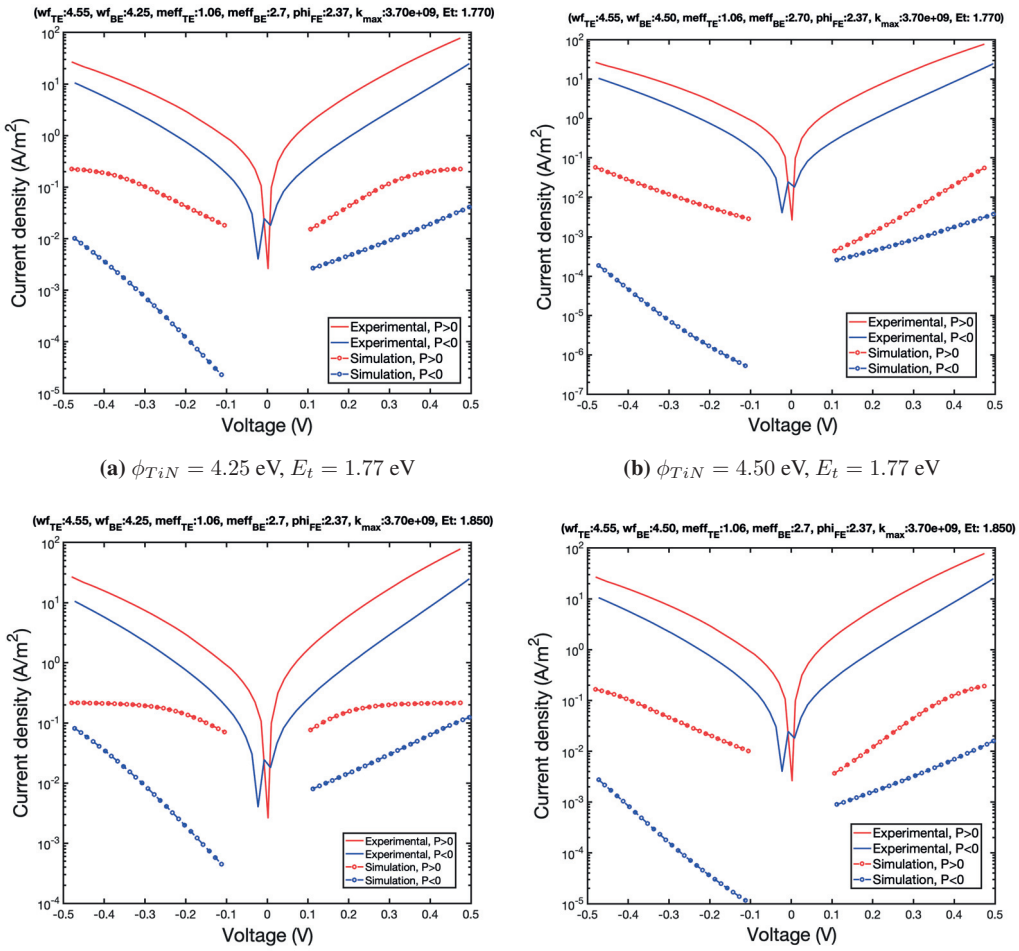

(a) $\phi_{TiN} = 4.25$ eV, $E_t = 1.77$ eV

(b) $\phi_{TiN} = 4.50$ eV, $E_t = 1.77$ eV

(c) $\phi_{TiN} = 4.25$ eV, $E_t = 1.85$ eV

(d) $\phi_{TiN} = 4.50$ eV, $E_t = 1.85$ eV

Figure 4.10: J-V plots for different E_t and ϕ_{TiN} values.

In research on similar devices findings show that the most probable mechanism for TAT is trap-to-trap tunneling and that the in-going current rate is the limiting rate for the overall current [31][38]. In the work of Athle et al. it was shown that the current was limited by thermal excitation to a trap state at 1.2 nm and 0.4 nm into the HZO from TiN and W respectively with $E_t = 1.77$ eV [24]. Attempts were made to implement these concepts into the TAT model already developed. The results are displayed below in figures 4.11a and 4.11b. In figure 4.11a the TAT code with only the in-going current considered is displayed and in figure 4.11b in-going current for trap states at 2nm into the HZO for TiN and W is displayed but with the current adjusted so the J-V curves could

be compared. Due to the poor results this attempted was not developed further.

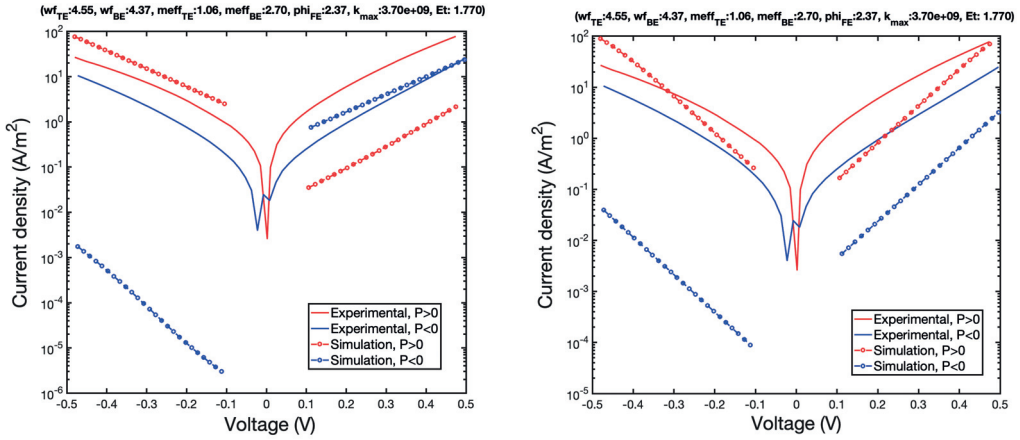

Figure 4.11: (a)J-V plot for TAT current with only in-going current considered (b) J-V plot based with only in going current for single trap states with the current multiplied by 10^3.

4.4 Introduction of empirical constants

The last simulations that were performed included an empirical constant, on for each current direction labelled $\alpha_{BE,TE}$ depending on the side the current was travelling from. The empirical constants are intended to account for the physical effects neglected in the model, due to its simplicity, in order to be able to perform accurate fitting to experimental data for the TAT. The simulations were performed with the initial values found in tables 2.1 and 2.2 except $\kappa_{max} = 3.7 \cdot 10^9\ m^{-1}$. The initial parameters for the TAT current were set to $E_t = 1.77$ eV, $N_t = 10^{27}$ m^{-3} and $x_T = 1$ nm, as these were the reasonable physical parameters which resulted in the highest current values for the TAT current, without the empirical constants. The two most accurate fits that were achieved for the TAT current and are displayed in figures 4.12a and 4.12b. For both values of the workfunction the data is well fitted for the positive polarization and follows the experimental data well especially for $\phi_{TiN} = 4.25$ eV in figure 4.12b. The fitting parameters varied by the fitting function also could be sustained within a reasonable physical range. This points towards the fact that the equations governing the behaviour of the electrons in the metal and HZO are physically sound, despite the simplifications used, and that they in terms of magnitude and dependence upon the voltage and band structure indicate that the parameters implemented are accurate except for the probable nor-

malization error. Similar parameter values to those that are used in our simulations were used by Athle et al.[24] in order to model similar devices and proved accurate which again points towards a normalization error. Inaccuracies could also result from unreasonable number of subintervals used for the integration over x-position which would affect how the Fermi-Dirac distribution and $W_{c,e}(x, E)$ are balanced.

The negative polarization still shows poor fitting and the gap between the current of the two polarizations for negative biases remains. This asymmetry in the fitting indicates that there are physical phenomena omitted most likely due to the simple model for calculating the band structure, as mentioned before. If the poor J-V dependence was because of the model for calculating the tunneling rates, it would have been seen for the positive polarization as well.

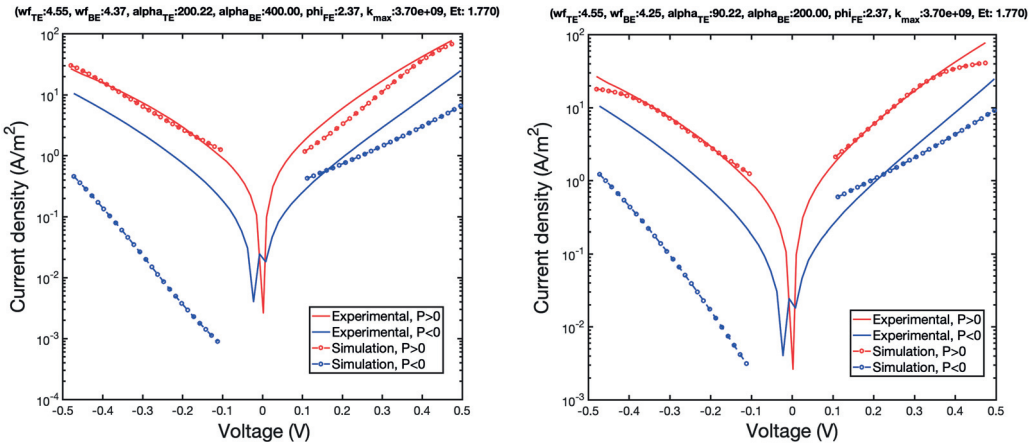

Figure 4.12: J-V plot for TAT current fit with (a) $\phi_{TiN} = 4.37$eV, $\alpha_{BE} = 400$, $\alpha_{TE} = 200.22$. (b) $\phi_{TiN} = 4.25$eV, $\alpha_{BE} = 200$, $\alpha_{TE} = 90.22$

The α constant for TiN is approximately two times higher that for the W. This is reasonable as the asymmetry in the physical properties of the metal will render different values that were omitted due to the simplicity of the model implemented. The size of the α constants point towards the fact that the simulated current levels were not unreasonably deviant which could be explained by a too simple model of the bandstructure, normalization and other omitted physical phenomena in the FTJ. Another explanation behind the results and behaviours relating to bandstructure is the possibility that TiO_x was formed between the TiN and HZO in the experimental data which is not

accounted for in any way in the model of the TAT. However this would affect both polarization directions and worsen the fit for both polarization states.

Fitting attempts that included both current mechanisms were also performed. The best result is shown in figure 4.13. From the result one could observe that the matching is quite poor even though the data was automatically fitted. The parameters that the fitting function changed were $\phi_{TiN} = 4.23$ eV and $E_t = 1.807$ eV. The α constants were found to be 75.15 for right-going current (positive voltages) and 13.22 for left-going current (negative voltages). These values do not match the ones from the simulations of the TAT current only. This is due to the fact that the fitting program manipulates parameters in order to fit both current mechanism to the data which worsens the fit for the TAT current. The fit also suffers from the poorly fitted transmission current for voltages higher than 50 mV which causes the discontinuities in the data, as the TAT current is more accurate for higher voltages. Both models have shortages and the simplified bandstructure calculation most likely is the key factor that affects them both in a negative way, causing the deviating on/off ratios in both cases and poor J-V dependence. Therefore it is hard to produce a good fit including both current models, hence, giving the poor result.

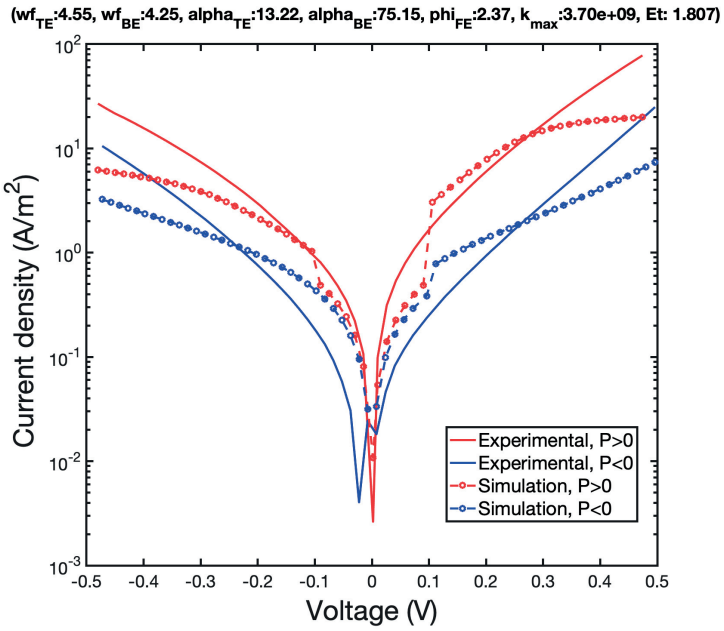

Figure 4.13: J-V plot for transmission and TAT current fit to experimental data.

To summarize the model is too simplified in order to match and fit the experimental data well.

Improvement of the TAT model based upon Jimenez-Molinos et al.[35] would involve a more complex band structure estimation in order to improve the current voltage dependence. Implementing Gaussian distribution for the trap states and modelling the trap-to-trap tunneling would also most likely greatly improve the accuracy and validity of the model used leading to improved current density levels.

Chapter 5

Conclusions

In the evaluation of the first model the main issue was to identify the non-zero current when the voltage applied over the FTJ was 0V. The analysis showed that the rate equations (equations 2.24 and 2.25) were constructed in such way causing the transmission rate of the in-going current, R_1, to become the decisive term in the expression for the total current. Due to this result new more accurate expressions for the rate equations were implemented.

The new rate equations based upon Jimenez-Molinos et al. after series of improvements resulted in a significantly lower current level compared to experimental data. The simulations also displayed poor current voltage dependence especially for the negative polarization direction and negative biases. Through improvement and fitting of the current levels. Empirical constants were lastly introduced which allowed for accurate fitting. The results indicated that the bandstructure calculation used in the model was too simple as the simulations for negative polarization direction displayed poor J-V dependence but not the positive direction. The low current levels could also be explained due to normalization errors or oversimplifications of the trap states and the current mechanism regarding them. However the good fit for positive polarization when including empirical constants indicates that the initial parameters used are accurate and that the equations describing the nature of electron transport are physically viable. But in general the model quite simply involves too many simplifications to properly model the physics of the FTJ device.

In order improve the TAT model based upon Jimenez-Molinos et al.[35] a more complex bandstructure estimation is needed. Using a Gaussian distribution for the trap states and modelling the trap-to-trap tunneling would also most likely greatly improve the accuracy and validity of the model used.

Bibliography

[1] M. Bahi and C. Eisenbeis, ”High Performance by Exploiting Information Locality through Reverse Computing,” 2011 23rd International Symposium on Computer Architecture and High Performance Computing, 2011.

[2] Abu Sebastian, Manuel Le Gallo, Geoffrey W. Burr, Sangbum Kim, Matthew BrightSky, and Evangelos Eleftheriou , ”Tutorial: Brain-inspired computing using phase-change memory devices”, Journal of Applied Physics 124, 111101, 2018.

[3] Garcia, V., Bibes, M. Ferroelectric tunnel junctions for information storage and processing. Nat Commun 5, 4289, 2014.

[4] T. Mikolajick, U. Schroeder and S. Slesazeck, ”The Past, the Present, and the Future of Ferroelectric Memories,” in IEEE Transactions on Electron Devices, vol. 67, no. 4, pp. 1434-1443, April 2020.

[5] R.B. Laibowitz, L. Esaki, P.J. Stiles. Electron transport in Nb-Nb oxide-Bi tunnel junctions. Physics Letters A, Volume 36, Issue 5, 1971.

[6] Günter Grossman. Fasta tillståndets fysik. Lunds Universitet. 2020

[7] Sólyom J. Free-Electron Model of Metals. Fundamentals of the Physics of Solids (9783540853152), 2009.

[8] N. W. Ashcroft and N. D. Mermin, Solid State Physics. Brooks- Cole, Belmont, MA, 1976.

[9] Loucks, T. L. Fermi Surfaces of Cr, Mo, and W by the Augmented-Plane-Wave Method. Phys. Rev.139,4A, A1181–A1188, 1965.

[10] Robin Athle, Anton E.O Persson, Andrea Troian, and Mattias Borg. Supporting information: Top Electrode Engineering for Freedom in Design and Implementation of Ferroelectric Tunnel Junctions Based on Hf1–xZrxO2 ACS Applied Electronic Materials 2022 4 (3), 1002-1009.

[11] Sciencing. ”What Type of Bonding Occurs in Tungsten?” 25 Apr. 2017, https://sciencing.com/type-bonding-occurs-tungsten-8365093.html. Accessed (2022-05-23)

[12] Angstrom Sciences Elements, ”Density of Elements Chart”, https://www.angstromsciences.com/density-elements-chart. Accessed (2022-05-23)

[13] ”Chemical elements of the periodic table sorted by Atomic Mass.” https://www.lenntech.com/periodic/mass/atomic-mass.htm. Accessed (2022-05-23)

[14] C.G.H. Walker, J.A.D. Matthew, C.A. Anderson, N.M.D. Brown, An estimate of the electron effective mass in titanium nitride using UPS and EELS, Surface Science, Volumes 412–413, 1998.

[15] Kittel C, McEuen P. Introduction to Solid State Physics. 8. ed. Wiley; 2005.

[16] Pantel, D.; Alexe, M. Electroresistance Effects in Ferroelectric Tunnel Barriers. Phys. Rev. B - Condens. Matter Mater. Phys. 2010, 82, 134105.

[17] Sze SM, Lee MK. Semiconductor Devices: Physics and Technology. 3. ed. Wiley-Blackwell; 2012.

[18] Solid Surface Physics. 1st ed. 1979. Springer Berlin Heidelberg; 1979.

[19] Michaelson, H. B. The Work Function of the Elements and Its Periodicity. J. Appl. Phys. 1977, 48 (11), 47294733.

[20] Ambriz-Vargas et.al. A Complementary Metal Oxide Semiconductor Process-Compatible Ferroelectric Tunnel Junction. ACS Applied Materials Interfaces 2017 9 (15), 13262-13268.

[21] Mitsui T. Ferroelectrics and Antiferroelectrics. In: Martienssen W., Warlimont H. (eds) Springer Handbook of Condensed Matter and Materials Data. Springer Handbooks. Springer, Berlin, Heidelberg. 2005.

[22] Mikolajick et al. IEEE Trans. Electron Dev. 2020, Pêsic et al. J. Comp. Electron. 2017.

[23] Griffiths, D. Introduction to Electrodynamics (4th ed.). Cambridge: Cambridge University Press. 2017.

[24] Robin Athle, Anton E.O Persson, Andrea Troian, and Mattias Borg. Top Electrode Engineering for Freedom in Design and Implementation of Ferroelectric Tunnel Junctions Based on Hf1–xZrxO2 ACS Applied Electronic Materials 2022 4 (3), 1002-1009.

[25] S. A. Vitale, J. Kedzierski, P. Healey, P. W. Wyatt and C. L. Keast, ”Work-Function-Tuned TiN Metal Gate FDSOI Transistors for Subthreshold Operation,” in IEEE Transactions on Electron Devices, vol. 58, no. 2, pp. 419-426, Feb. 2011.

[26] Davies, J. The Physics of Low-dimensional Semiconductors: An Introduction. Cambridge: Cambridge University Press. 1997.

[27] Yue Peng, Genquan Han, Wenwu Xiao, Yan Liu, Qinglong Li, Chunfu Zhang, Jincheng Zhang, Yue Hao, Band alignments at Hf1-xZrxO2/Si and Hf0.52Zr0.48O2/Si0.55Ge0.45 interfaces, Superlattices and Microstructures, Volume 130, 2019.

[28] Zhipeng Dong, Xi Cao, Tong Wu, and Jing Guo , ”Tunneling current in HfO2 and Hf0.5Zr0.5O2-based ferroelectric tunnel junction”, Journal of Applied Physics 123, 094501. 2018.

[29] Ohlén G. Kvantvärldens fenomen: teori och begrepp. Lund: Studentlitteratur; 2005.

[30] Fowler Ralph Howard and Nordheim L. Electron emission in intense electric fieldsProc. R. Soc. Lond. A119173–181. 1928.

[31] Shimeng Yu, Ximeng Guan, and H.-S. Philip Wong , ”Conduction mechanism of TiN/HfOx/Pt resistive switching memory: A trap-assisted-tunneling model”, Appl. Phys. Lett. 99, 063507. 2011.

[32] Mehta RR, Silverman BD, Jacobs JT. Depolarization fields in thin ferroelectric films. Journal of Applied Physics. 1973;44(8):3379-3385.

[33] R. Tsu and L. Esaki , ”Tunneling in a finite superlattice”, Appl. Phys. Lett. 22, 562-564. 1973.

[34] X. R. Cheng, Y. C. Cheng, and B. Y. Liu , ”Nitridation-enhanced conductivity behavior and current transport mechanism in thin thermally nitrided SiO2”, Journal of Applied Physics 63, 797-802. 1988.

[35] F. Jiménez-Molinos, F. Gámiz, A. Palma, P. Cartujo, and J. A. López-Villanueva , ”Direct and trap-assisted elastic tunneling through ultrathin gate oxides”, Journal of Applied Physics 91, 5116-5124. 2002.

[36] H. J. Reittu, ”Fermi’s golden rule and Bardeen’s tunneling theory”, American Journal of Physics 63, 940. 1995.

[37] Compendium, Quantum Mechanics FYSN17/FMFN01, Mathematical Physics, Last revision by Andreas Wacker February 13, 2013.

[38] Zhen Fan, Juanxiu Xiao, Jingxian Wang, Lei Zhang, Jinyu Deng, Ziyan Liu, Zhili Dong, John Wang, and Jingsheng Chen , ”Ferroelectricity and ferroelectric resistive switching in sputtered Hf0.5Zr0.5O2 thin films”, Appl. Phys. Lett. 108, 232905. 2016.

[39] S. Monaghan, P.K. Hurley, K. Cherkaoui, M.A. Negara, A. Schenk, Determination of electron effective mass and electron affinity in HfO2 using MOS and MOSFET structures, Solid-State Electronics, Volume 53, Issue 4, 2009.

[40] Anton E. O. Persson, Robin Athle, Johannes Svensson, Mattias Borg, and Lars-Erik Wernersson , ”A method for estimating defects in ferroelectric thin film MOSCAPs”, Appl. Phys. Lett. 117, 242902. 2020.

[41] Andreas Dörfler. ”Ferroelectric Tunnel Junctions: Models for Memory and Neuromorphic Applications”. PhD thesis. Universite du Quebec, Institut National de la Recherche Scientifique Centre Energie Materiaux Telecommunications. 2021.

[42] Kohlstedt H, Pertsev NA, Contreras JR, Waser R. Theoretical current-voltage characteristics of ferroelectric tunnel junctions. 2005.

Printed by Tryckeriet i E-huset, Lund 2022

LUND
UNIVERSITY

Series of Master's theses
Department of Electrical and Information Technology
LU/LTH-EIT 2022-874
http://www.eit.lth.se